metals

MDPI

Article

Tailoring Weldability for Microstructures in Laser-Welded Near-α Titanium Alloy: Insights on Mechanical Properties

Shiwei Zhang [1,*], Baoqiang Cong [2], Zhi Zeng [3], Ying Liu [1] and Lu Chai [1]

[1] Aeronautical Key Laboratory for Welding and Joining Technologies, AVIC Manufacturing Technology Institute, Beijing 100024, China
[2] School of Mechanical Engineering and Automation, Beihang University, Beijing 100191, China; congbq@buaa.edu.cn
[3] School of Mechanical and Electrical Engineering, University of Electronic Science and Technology of China, Chengdu 611731, China; zhizeng@uestc.edu.cn
* Correspondence: zswhit@outlook.com

Abstract: With the development of lightweight aerospace structures, the use of the high-quality and efficient laser welding of near-α titanium alloys has received widespread attention and favor thanks to its superior comprehensive performance. The welding experiment of 3 mm thick TA15 titanium alloy was carried out by YAG laser welding, and the material weldability, microstructure, microhardness, and mechanical properties of welded joints were systematically studied. The results indicated that laser welding of TA15 titanium alloy can produce well-formed welded joints without defects such as cracks and porosity. The welded metal used was a typical basket-weave microstructure composed of a large number of α′ martensitic phases and a small number of high-temperature residual β phases, and the heat-affected zone was a staggered arrangement of undissolved α phase and needle-like α′ martensite. The microhardness of the welded joint showed a hump distribution, and the hardness of WM fluctuated between 410 and 450 HV since the martensitic transformation occurred during the solidification of the weld under thermal cycling, and the β phase changed to the needle-like α′ phase. The tensile test indicated that the fracture position was located in the base metal area, and the fracture morphology showed the equiaxial dimple morphology of different sizes in a ductile fracture mode. The welded metal had the lowest impact performance (average value of 5.3 J) because the weld area was predominantly coarse α′ martensite. This experiment conducted systematic, in-depth, and extensive research on welding processes, hardness, tensile, impact, and fracture mechanisms. Based on the special product applications in the aerospace field, it was more targeted and conducive to promoting the application of the welding process in this material.

Keywords: laser welding; TA15 titanium alloy; weldability; mechanical properties

Citation: Zhang, S.; Cong, B.; Zeng, Z.; Liu, Y.; Chai, L. Tailoring Weldability for Microstructures in Laser-Welded Near-α Titanium Alloy: Insights on Mechanical Properties. *Metals* **2024**, *14*, 690. https://doi.org/10.3390/met14060690

Academic Editor: Masahiro Fukumoto

Received: 21 May 2024
Revised: 6 June 2024
Accepted: 9 June 2024
Published: 11 June 2024

1. Introduction

With the development of aerospace technology, titanium alloy [1,2], known as a modern metal and space metal, has gained increasing attention and favor in aerospace manufacturing due to its low density, high specific strength, strong damping performance, high impact toughness, and strong fatigue resistance [1]. As a form of near-α titanium alloy [3,4], TA15 titanium alloy combines the α phase, which has the weldability and thermal strength of titanium alloys, and the β phase, which possesses the plasticity of dual-phase titanium alloys and has been widely used in aircraft frame structural components [5–7]. In the manufacturing process of titanium alloy components for aviation, welding technology has become indispensable because welding structures are simple, material-saving, and have high reliability, which can achieve high-quality, efficient, and low-cost manufacturing [8,9]. However, because of the metallurgical properties of titanium alloys, welding defects such as pores and cracks are prone to occur during the welding process, which could cause stress

concentration, weaken the strength of the welded joints, reduce fatigue performance, and damage structural sealing performance [10].

Many advanced welding technologies such as friction stir welding, hybrid laser-arc welding (HLAW) [11], electron beam welding (EBW) [12], and laser beam welding (LBW) [13,14] have attracted attention to join titanium alloy. LBW, as one of these techniques, can provide favorable results for welding titanium alloy due to its rapid processing capability and precision [15–17]. Zhang et al. [18] investigated whether the residual stress distribution zone of laser beam-welded titanium alloy joints was lower compared to the traditional fusion welded joints. In addition, it has other advantages, such as high efficiency, low heat input, and small deformation. Xie [19] found out that weld quality underwent a significant improvement as plasma fluctuation was controlled in the laser welding process. Deng et al. [20] reported that the heat-affected zone (HAZ) of welded joints mainly consisted of α phase and acicular martensitic phase α′ in TA15 titanium alloy. Zhan et al. [21] used experimental and simulation methods to research TA15 titanium alloy joints welded by LBW, and the simulation results were consistent with the experimental results. Zhang et al. [18] also used laser-TIG hybrid welded Ti22Al–27Nb and TA15 dissimilar joints, and the results showed that the base metal near the TA15 alloy retained the lamellar structure, and the microstructure of the HAZ in TA15 alloy mainly consisted of acicular α′ martensite near the fusion line. Xu et al. [22] found that lamellar microstructures were composed of α laths (200–300 nm) and the retained β phases, increasing the elongation by 11.4%; this indicated that transformed α phases to a + β lamellar phases increased mechanical properties [22,23].

In order to enlarge the application of LBW in the connection of TA15 titanium alloy based on the high-quality and efficiency advantages of LBW, in this text, the weldability of 3 mm TA15 titanium alloy was investigated. The link between weld parameters and joint geometry was measured. To evaluate the weld quality, the microstructure, mechanical properties, and fracture mechanism are analyzed and discussed in detail.

2. Experimental Materials and Method

The material used was a TA15 titanium alloy (nominal composition Ti-6.5Al-2Zr-1Mo-1V) plate with dimensions of 200 mm × 100 mm × 3.0 mm. Its chemical composition is shown in Table 1. Before welding, ultrasonic cleaning and acetone wiping of the parts were performed to remove oil stains, and then the welding experiments were conducted.

Table 1. Chemical composition of TA15 alloy (wt%).

Al	V	C	Zr	Fe	O	Si	Mo	N	H	Ti
6.7	2.4	0.01	2.1	0.2	0.1	0.02	1.9	0.02	0.002	Bal.

The experiment system selected a fiber laser system from the German IPG company, with a Rayleigh length of 10.3 mm and a wavelength of 1.07 μm. Fiber diameter was 300 μm. The Precitec laser welding head (Germany) was jointly loaded on the KUKA robot (Germany), as shown in Figure 1a. In order to protect the laser system, it was tilted 10 degrees, and the defocus amount used was +20 mm to reduce the undercut tendency. The other welding parameters are shown in Table 2.

After the experiment, TA15 titanium alloy test plates were cut to obtain metallographic samples, microhardness samples, and tensile and impact samples. The experimental trials were as follows in Figure 1b. The tensile sample sizes of the base material and welded joints are shown in Figure 2a. The metallographic and SEM microstructures were etched using Keller reagents (HF: HNO_3: H_2O = 1:5:44). SEM and EBSD were tested by Apreo C Thermo Fisher Scientific America. Phase analysis of the welded joint was accurately analyzed qualitatively and quantitatively using an X-ray diffractometer (XRD), with a testing parameter of angle range 2θ:20–100° with a scanning step size of 0.02°. Microhardness was tested at intervals of 0.15 mm along the cross-section of the weld seam and a 300 g force for 15 s. The room temperature tensile test was conducted on a CMT 5205GL test machine with a loading

tensile rate of 0.5 mm/min. An optical extensometer was used to measure the elongation of materials in this experiment. Ultimate tensile strength (UTS), yield strength (YS), and elongation (A%) were measured. The fracture morphology was observed using SEM to analyze its fracture mechanism. According to GB/T 2650-2008 "Impact Test Methods for Welded Joints", small-sized 10 × 2.5 × 55 Charpy impact specimens were performed at different positions of the welded joint (weld metal, heat-affected zone, and base material), as shown in Figure 2b. Three specimens were used for both tensile and impact tests to verify the reliability of the data. And all tensile and impact specimens were milled flat to maintain thickness consistency. Impact tests at room temperature were conducted to analyze the plasticity and toughness of the welded joint.

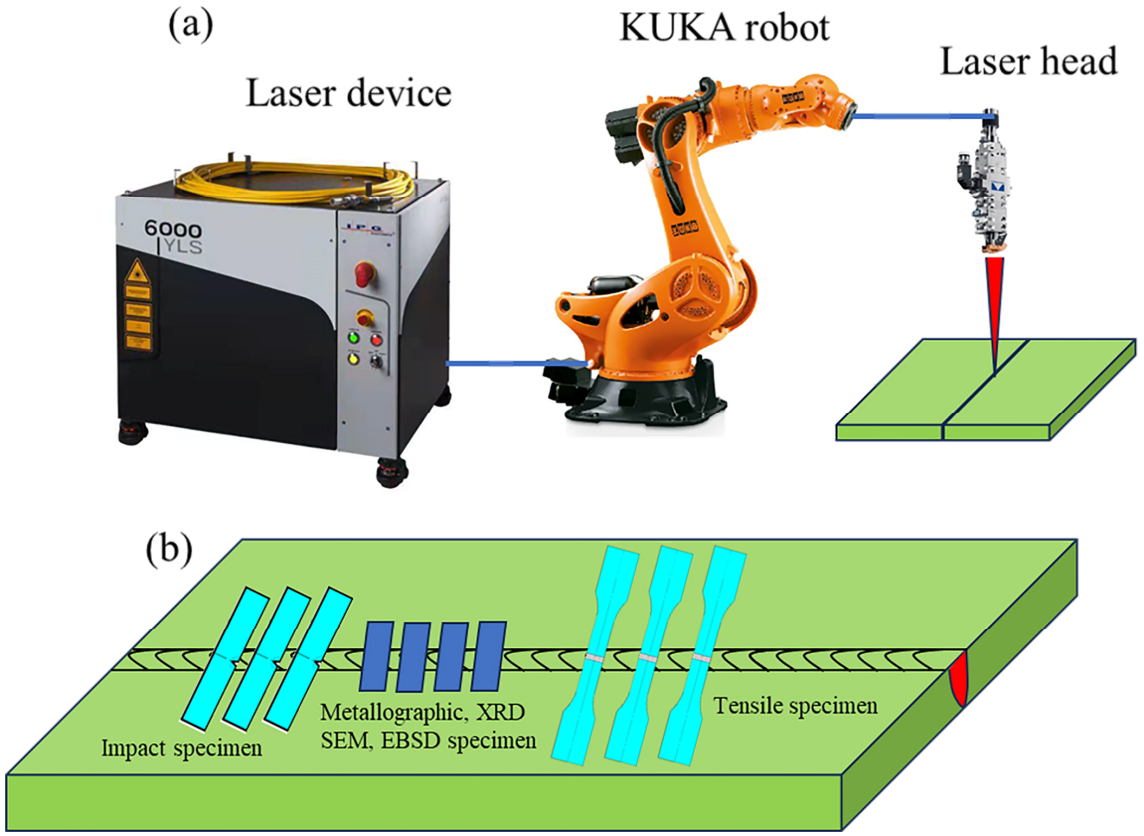

Figure 1. Schematic of welding machines and experimental trials. (**a**) welding machines; (**b**) experimental trials.

Table 2. Welding process parameters.

No.	Laser Power	Welding Speed	Defocus Amount
	P/kW	*v*/(m/min)	*F*/mm
1	2.2	1.2	+20
2	2.5	1.2	+20
3	2.8	1.2	+20
4	3.0	1.2	+20
5	3.2	1.2	+20
6	3.0	1.8	+20
7	3.0	1.5	+20
8	3.0	0.9	+20

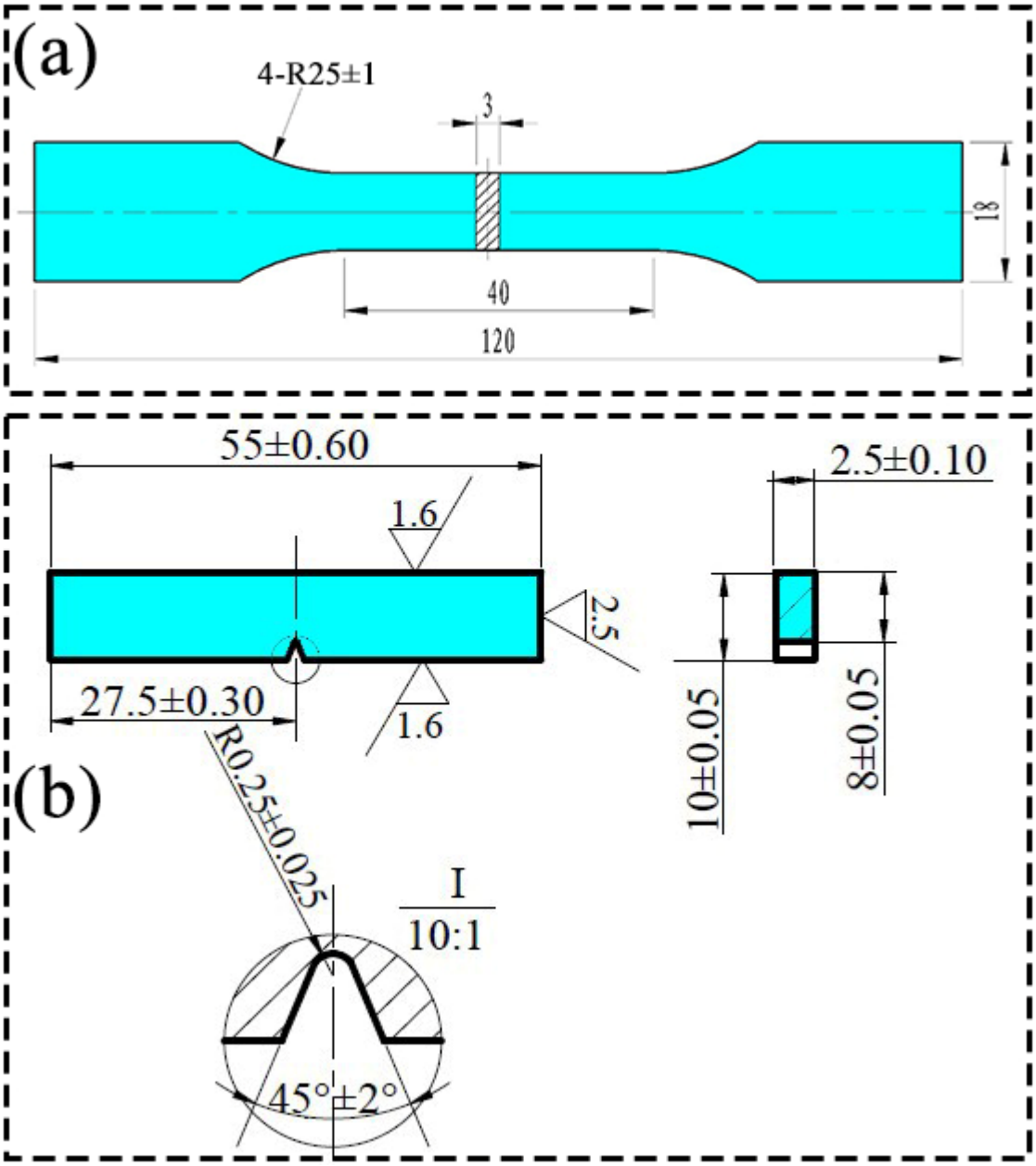

Figure 2. Schematic of tensile and impact specimen: (**a**) tensile specimen; (**b**) impact specimen.

3. Results and Discussion

3.1. Weldability Analysis

The effects of laser power on the welded seam formation (front and back surface) are shown in Figure 3, and the depth penetration and weld width of welded joints are shown in Figure 4, respectively. When the welding speed remained constant (v = 1.2 m/min), as the laser power (P < 2.8 kW) increased, the penetration depths progressed from incomplete penetration to burning through, resulting in undercut [24], as shown in Figure 3. The increase in welded width of the weld seam followed an approximately linear pattern, as shown in Figure 4. The photoinduced plasma impacted the keyhole, which caused the reaction and the spreading of the metal liquid around the keyhole towards the width of the molten pool [14]. As the laser power was 3.0 kW, the welded seam was vivid and lustrous, and there were no defects, such as spatters on the surface. As the laser power continued to increase, severe spatters occurred on the front, and collapse appeared on the back [25].

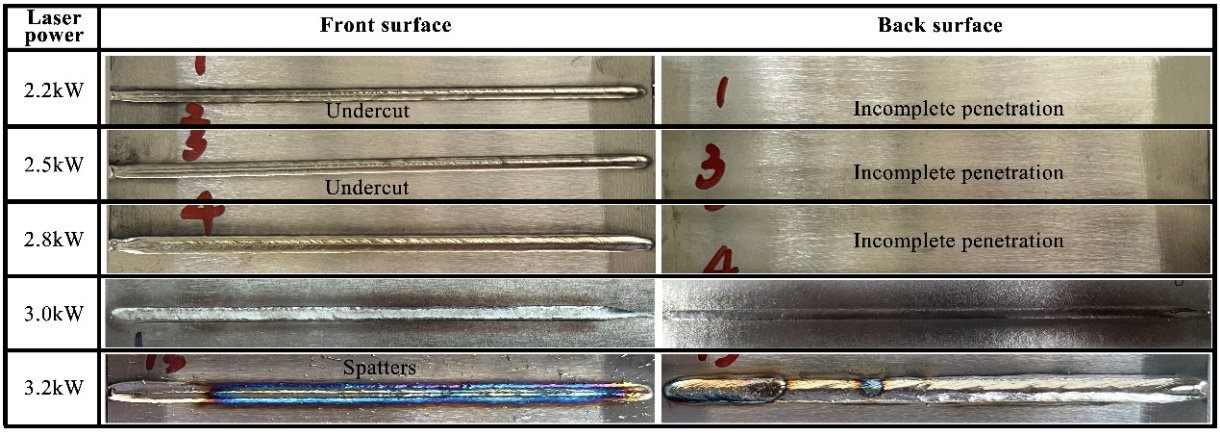

Figure 3. The influence of laser power on the welded seam formation.

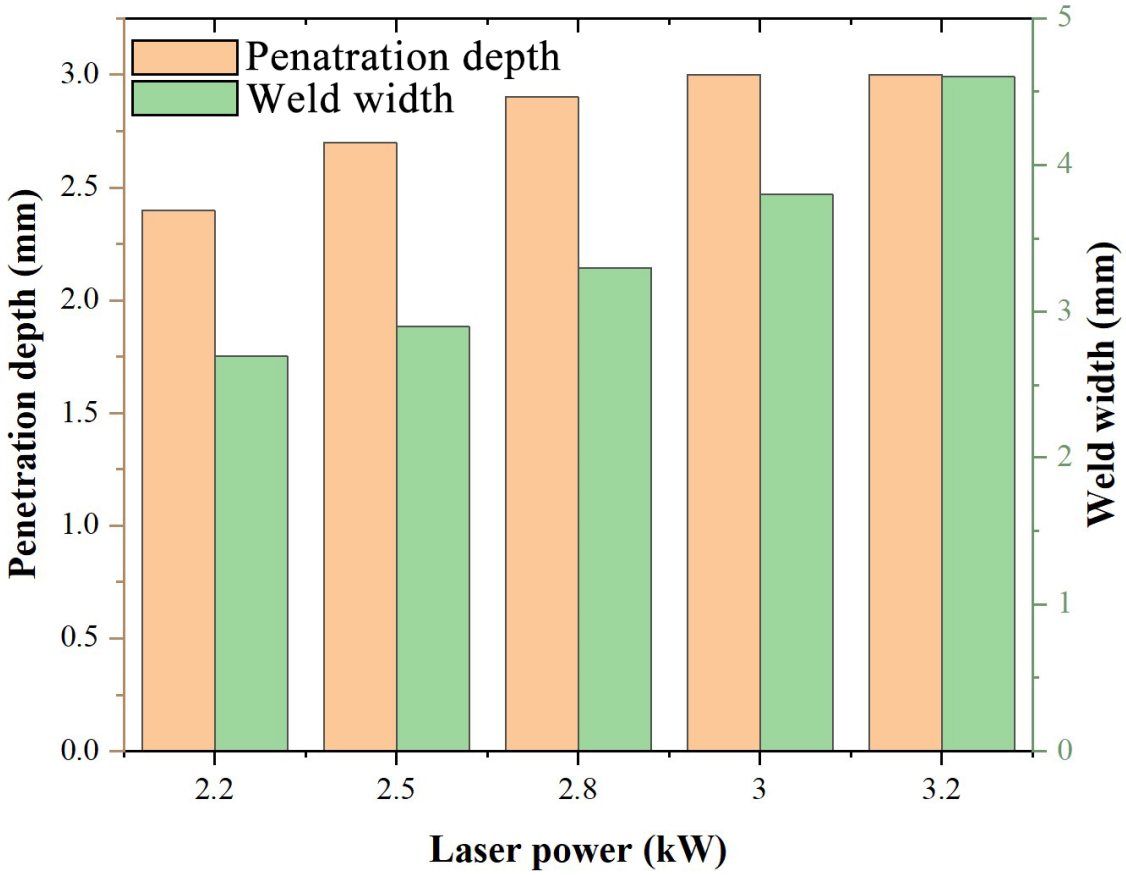

Figure 4. Effects of laser power on the depth penetration and weld width of the welded joints.

Figures 5 and 6 show the effect of welding speed on the welded seam formation (front and back surface) and the depth and width of weld penetration in welded joints, respectively. The nominal heat input (*HI*) of laser welding is expressed as follows [26]:

$$HI = 60P/v \quad (1)$$

where P is laser power (kW), and v is welding speed.

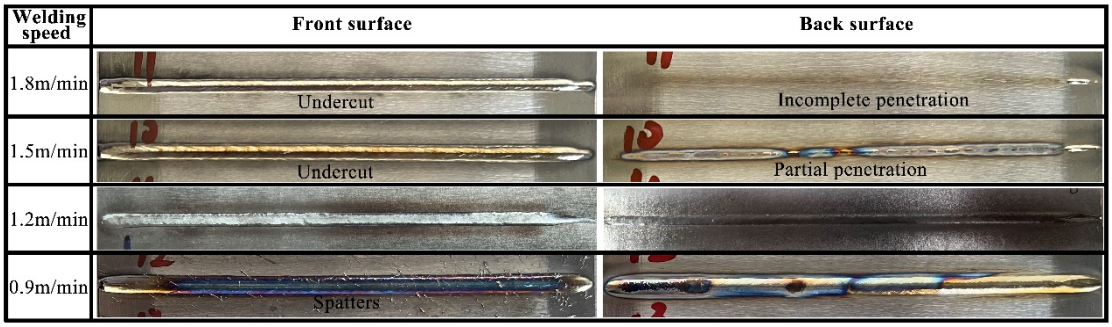

Figure 5. The influence of welding speed on the welded seam formation.

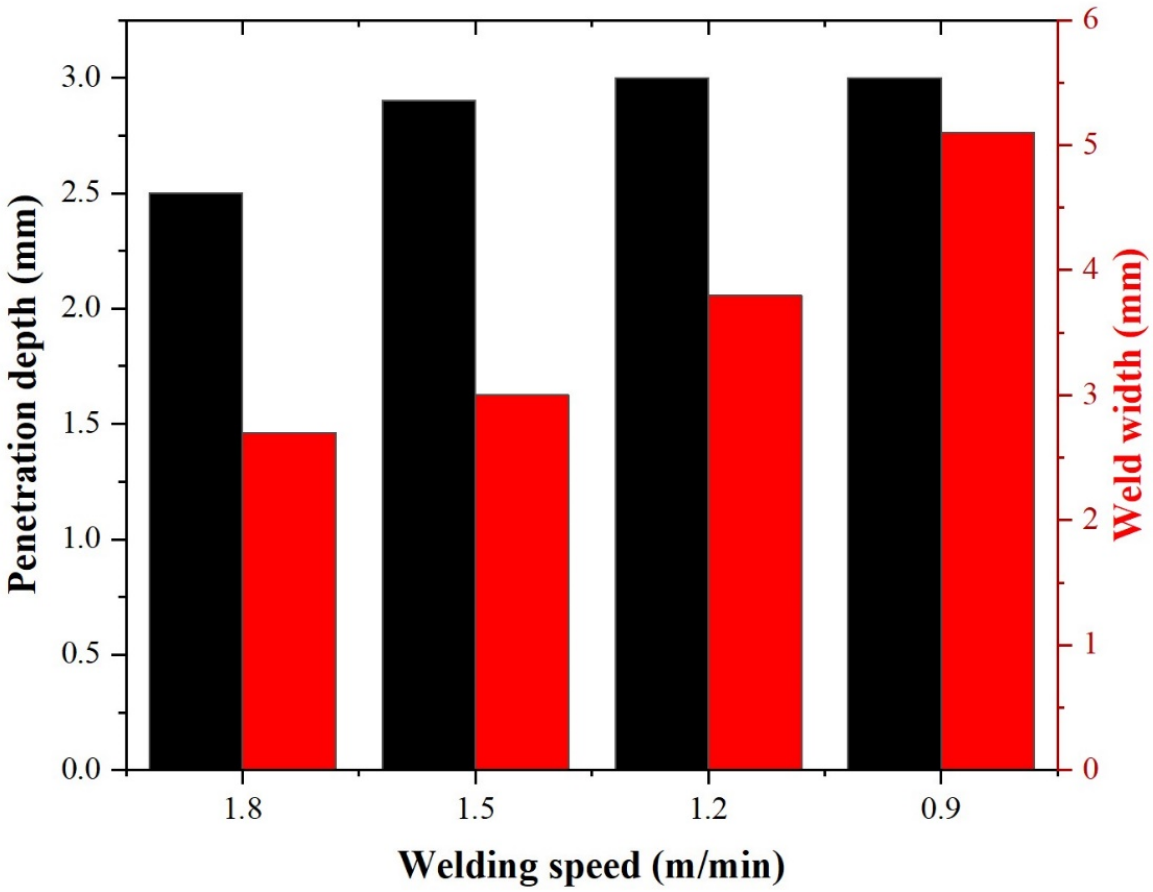

Figure 6. Effects of welding speed on the depth penetration and weld width of the welded joints.

From the above Equation (1), it can be seen that welding speed and laser power had a reverse effect on the welded seam formations [27]. When the welding speed was too high, the weld seam was not fully penetrated, and there were undercut defects on the surface of the weld seam. As the welding speed decreased, the depth and width of the weld seam gradually increased. After welding process optimization, when the laser power (P) was 3.0 kW, the welding speed (v) was 1.2 m/min, and the defocus (F) was +20 mm, the welded joint could be obtained with good macroscopic morphology and beautiful forming. The weld seam was smooth and flat, and there were no defects, such as spatters and cracks on the weld surface, as shown in Figure 7a,b. X-ray inspection results for laser-welded TA15 joints showed that the weld seam was well formed and there were no internal defects such as pores, cracks, or incomplete penetration, as shown in Figure 7c.

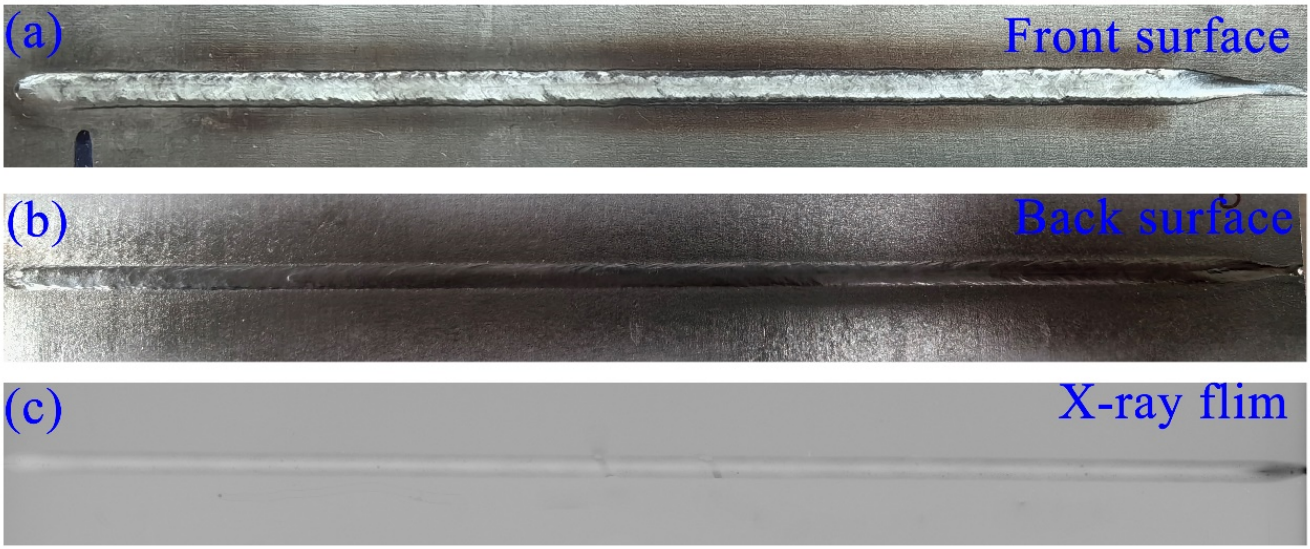

Figure 7. Macro-morphology and X-ray inspection image of welded joints: (**a**,**b**) front surface and back surface morphology and (**c**) X-ray film. (Experimental parameters: P = 3.0 kW, v = 1.2 m/min, F = +20 mm).

3.2. Microstructure of the Welded Joint

Figure 8 shows the macro-morphology of the welded joint and SEM images of different regions under optimal process parameters. Figure 8a shows the microstructure of the welded joint divided into the following three regions: the welding metal zone (WZ), the heat-affected zone (HAZ), and the base metal (BM) [8,20]. The regions were symmetrical left and right, with the weld seam as the center.

By zooming in on different regions of the welded joint through SEM photos, the microstructure of the welded metal underwent rapid melting and cooling under the high-speed and high-temperature action of laser welding, forming coarse columnar grains [15], as shown in Figure 8b, and forming single α plate bodies; the size of the crystal cluster α phase was small because there was not enough time for the β phase to transform into the equilibrium α phase through diffusion [28]. Instead, it was through the regular short-range migration of atoms that shear transformation was achieved, forming interlaced needle-like martensitic phases. The crystal clusters that nucleated at the grain boundaries could not fill the entire interior of the grain and instead nucleated at the interfaces of other crystal clusters. To minimize the total nuclear energy, the new α plate bodies were in contact with existing plate α in a dotted manner, and nucleation and growth were in progress on the phase surface. This microstructure was a typical basket-weave microstructure [29]. Due to the fast-cooling rate of laser welding, long needle-shaped martensite was generated. The martensite phase α inside had a large aspect ratio and a width of the submicron level, and the plates consisted of deformed bodies with different Bulger's orientation relationships [30]. For the heat-affected zone in Figure 8e, the microstructure affected by heat underwent element diffusion under the action of a welding thermal cycle, where the parallel layer α phase in the transformed group β dissolved [30], as shown in Figure 8f. The internal equiaxed α phase transferred towards a short rod shape, and element diffusion occurred between equiaxed α and β transformed textures [31,32], as shown in Figure 8f. Figure 8h demonstrates how BM was a typical α + β bimodal structure, accounting for about 14.7%. The thickness of the parallel layer α phase in the β transformed structure was about 1–2 μm, as shown in Figure 8i,j.

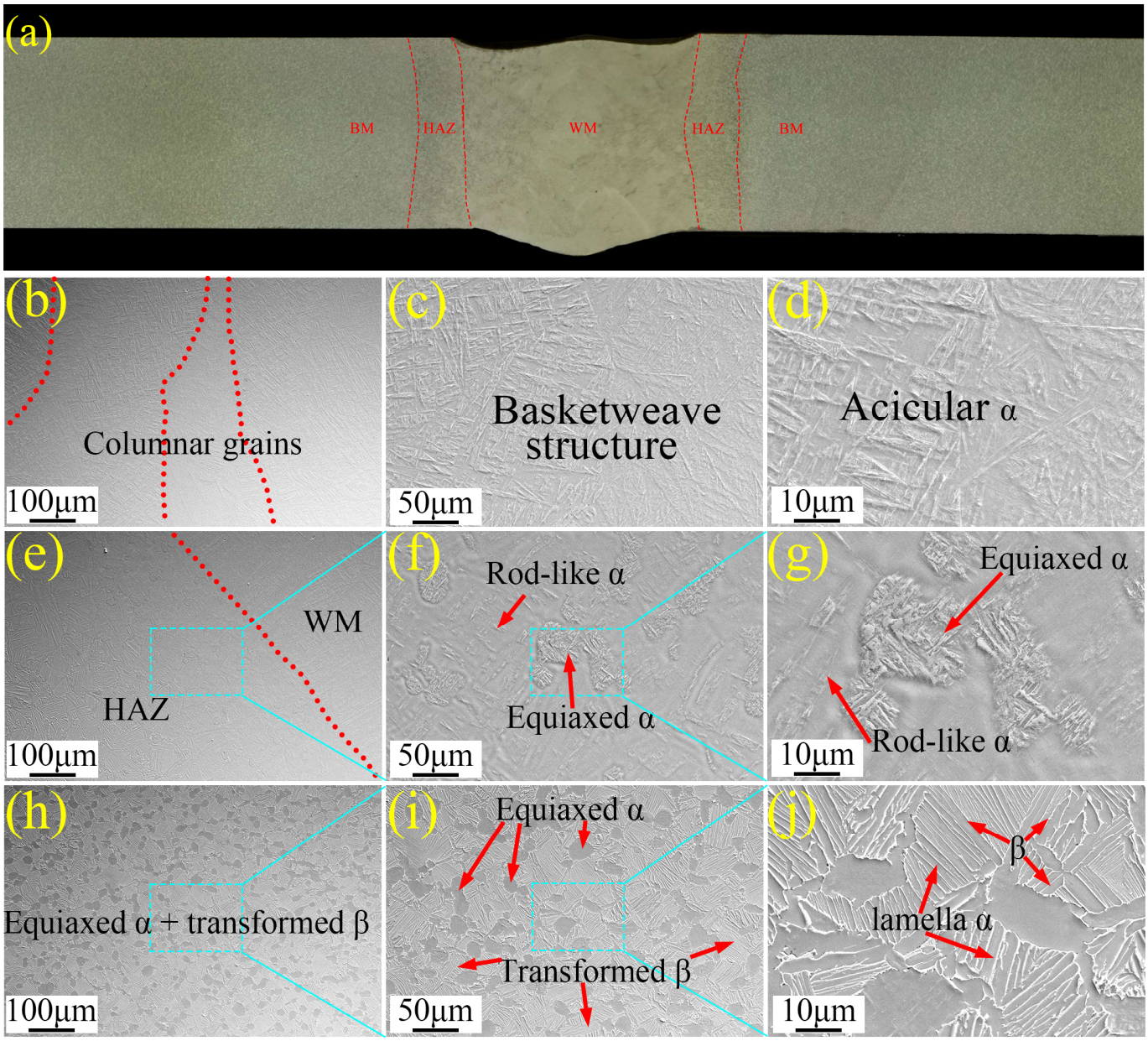

Figure 8. Macro-morphology of the welded joint and SEM images of different regions: (**a**) Macro-morphology of welded joint; (**b**–**d**) SEM images of welded metal (WM); (**e**–**g**) SEM images of the heat-affected zone (HAZ); and (**h**–**j**) SEM images of base metal (BM). (Experimental parameters: P = 3.0 kW, v = 1.2 m/min, F = +20 mm).

There was a significant difference in crystal orientation in the IPF of welded metal, resulting in a strong texture, as shown in Figure 9a. The pole figure shows that the maximum intensity of the welded metal was 27.757 in Figure 9d, which far exceeded 12.232 of HAZ in Figure 9e and 9.358 of BM in Figure 9f. This indicates that the microstructure of the welded metal occurred with the β → α phase transition during the solidification process, which followed the Bulger's orientation relationship [33], namely <110> β // (0001) α, <111> β // <2-1-1> α; therefore α inherited β orientation from phases. The SEM results in Figure 8b–d indicate that the β phase grains were large in the WM region; therefore, there was a strong phase transition texture at the WM region, as shown in Figure 8 [34,35]. There was no significant solidification process in HAZ. However, under the action of thermal cycling, the microstructure underwent a partial transformation, so the IPF of HAZ in

Figure 9b shows that the characteristics of the microstructure were between the WM and BM regions, so there was little change in the microstructure of HAZ and BM. From the IPF in Figure 9b,c, it can be seen that the colors were relatively uniform; no significant preference orientation existed, indicating that the texture intensity of HAZ and BM was equivalent.

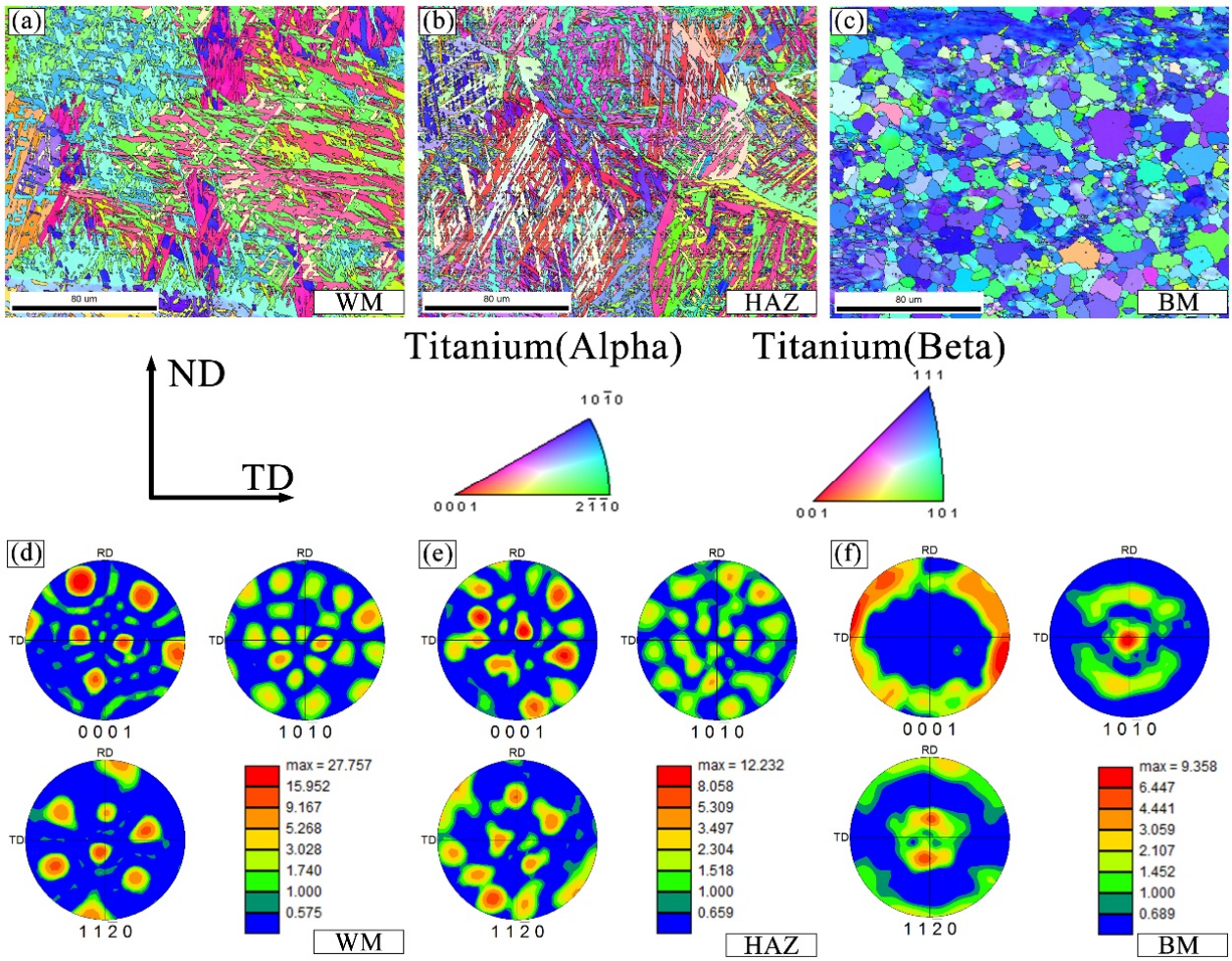

Figure 9. EBSD analysis of different areas of welded joints. (**a**) IPF of WM; (**b**) IPF of HAZ; (**c**) IPF of BM; (**d**) PF of WM; (**e**) PF of HAZ; and (**f**) PF of BM. (Experimental parameters: P = 3.0 kW, v = 1.2 m/min, F = +20 mm).

3.3. XRD Phase Analysis

Figure 10 shows the XRD phase composition results of the welded metal zone and base metal under the optimal process parameters. The spectrum of the base metal mainly included the diffraction peak of α phase and β phase. While the welded metal zone mainly included α′ phase diffraction peaks of different crystal planes in the martensitic phase and the diffraction peak of the weak β phase, the harmful phase did not occur, indicating that the rapid cooling of the high-temperature melt inside the weld pool during the welding solidification stage was caused by the shear transformation α′ phase [36]. There was still a small amount of high-temperature retention for martensitic phase β at the boundary [37]. A large number of α′ martensite phases increased the microhardness and tensile strength of the welded joints.

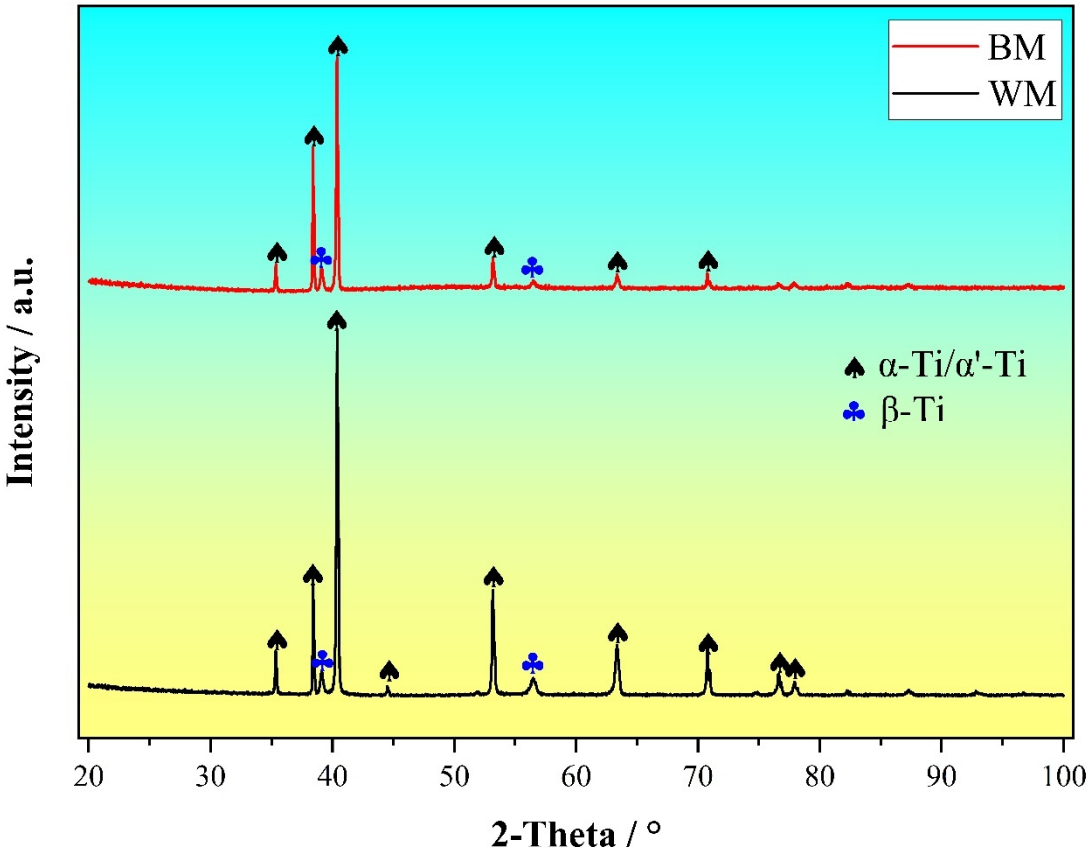

Figure 10. XRD pattern of welded metal and base metal. (Experimental parameters: P = 3.0 kW, v = 1.2 m/min, F = +20 mm).

3.4. Microhardness

Figure 11 shows the microhardness distribution of laser-welded joints under optimal process parameters. To some extent, it reflects the deformation and failure ability of welded joints under external forces. The microhardness values of the base material were the lowest, and the average value was about 340 HV. The microhardness near the edge of the heat-affected zone was the highest, and the value was 454 HV. The hardness of the welded metal fluctuated between 410 and 450 HV. Because under the thermal cycling effect of high-speed laser welding, there were fluctuations in composition and energy leading to martensitic transformation during the solidification of the welded zone, the β phase was transformed to the needle-shaped α′ phase, which caused differences in microhardness [36]. Combining the microstructure and XRD analysis, it can be confirmed that a large number of needle-like structures with high dislocation density and twinning were α′-phase-formed in the welded metal zone.

3.5. Mechanical Properties

The tensile properties of welded joints and the base metal under the optimal process parameters are shown in Table 3. The ultimate tensile strength (UTS) of the welded joint was 1006 ± 8.5 MPa, the yield strength (YS) was 935 MPa, and the elongation was 13% ± 1.2%. The tensile strength of the base metal was 994 MPa, the yield strength was 931 MPa, and the elongation was 14% ± 0.8%. The fracture positions were all located in the base metal area. The comparative tensile results show that the tensile strength of welded joints was greater than that of the base metal.

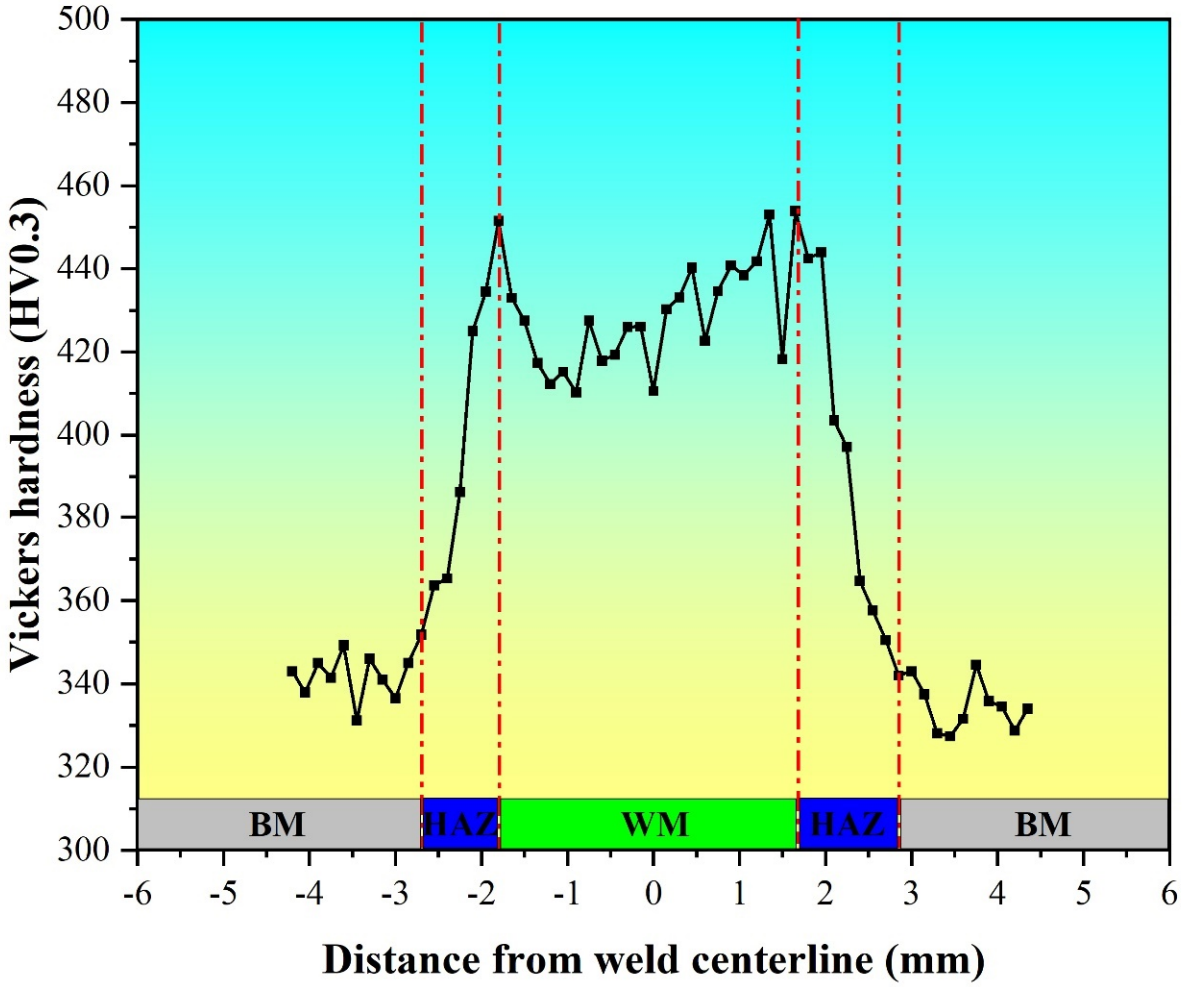

Figure 11. Microhardness distribution of welded joints. (Experimental parameters: P = 3.0 kW, v = 1.2 m/min, F = +20 mm).

Table 3. Tensile properties of welded joints and base metal.

Material	UTS	YS	Elongation	Fracture Location
	MPa	MPa	%	
Base metal	994 ± 5.6	931 ± 4.7	14 ± 0.8	Base metal
Welded joint	1006 ± 8.5	935 ± 5.6	13 ± 1.2	Base metal

Both the base metal and the welded joint specimens underwent surface necking due to the nucleation and growth of micropores under tensile stress [38], followed by the aggregation and growth of micropores, and finally, fracture, with a fracture angle of about 45°, as shown in Figure 12. The tensile specimens are generally fractured in the base material, and this indicates that equal-strength-matched welded joints were obtained.

Figure 13 shows the morphologies of the tensile fracture surface, which exhibited typical ductile fracture characteristics, such as tearing ridges and dimples of varying sizes, as shown in Figure 13a,b. Further explanation indicates that the fracture process belonged to the mechanism of microporous aggregation fracture [38], as shown in Figure 13c,d. This indicates that laser welding can produce welding joints with superior mechanical properties and obtain fracture morphology with ductile dimple characteristics.

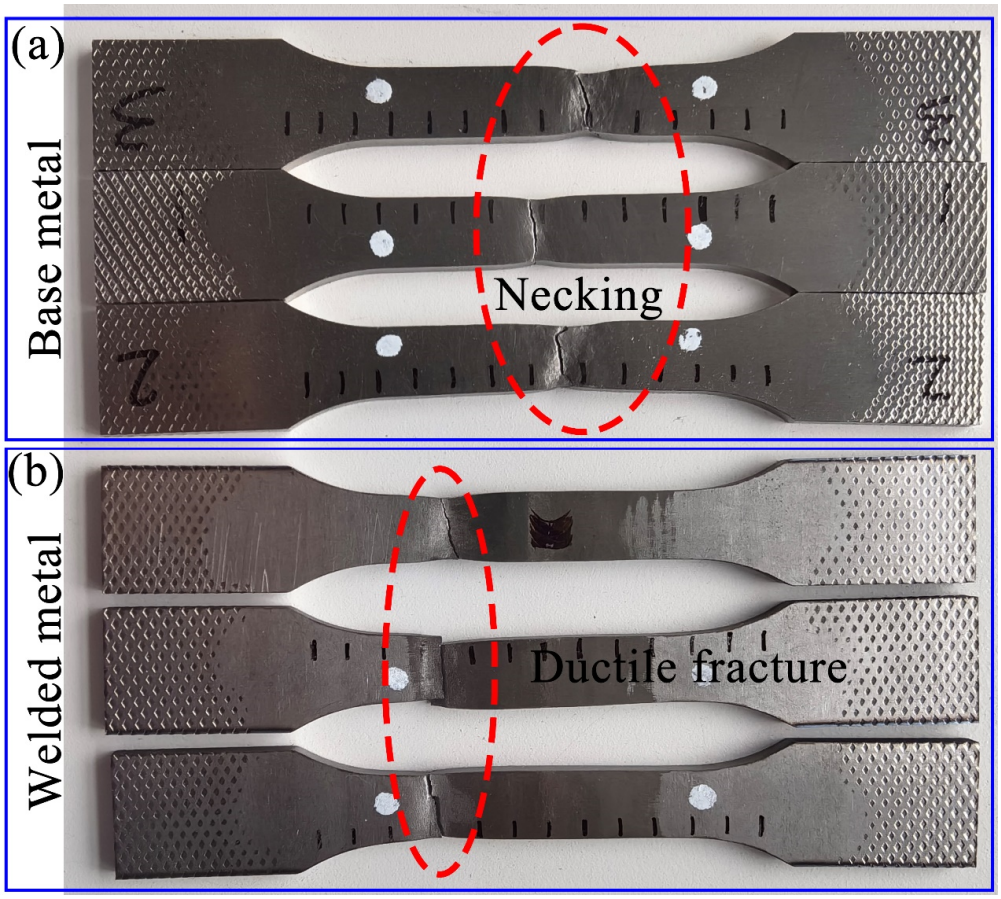

Figure 12. Macro-morphologies of tensile specimens after fracture. (**a**) base metal tensile specimens; (**b**) welded metal tensile specimens. Red circles indicated necking and the location of fracture. (Experimental parameters: P = 3.0 kW, v = 1.2 m/min, F = +20 mm).

According to GB/T 2650-2008 "Impact Test Method for Welded Joints" [39], tests were conducted on different positions of the welded joint (base metal, heat-affected zone, and welded metal), with three specimens for each position. The test results of the impact properties are shown under optimal process parameters in Figure 14. The average impact property of the base metal was 8.6 J, which was higher than that of the heat-affected zone and welded metal. The average value of the weld metal that had the lowest impact performance was 5.3 J. This was because the impact properties were closely related to the corresponding microstructure, and the base metal area was mainly composed of small α + β bimodal microstructures [40,41], where the thickness of parallel layers α was approximately 1–2 μm. And the welding metal zone was mainly coarse α′ martensite, while the average impact performance of the heat-affected zone was 7.2 J due to partial microstructure evolution in the heat-affected zone, resulting in higher performance.

In order to explore the reasons for the lowest impact performance of the weld metal zone, the surface morphology of the impact fracture of the weld metal zone was mainly analyzed under optimal process parameters. Among them, Figure 15a,b shows that the macroscopic fracture surface appeared dark gray. It consisted of three parts (source region, radiation region, and shear lip region). The crack source region was near the notch, as shown in Figure 15a. Microscopic fracture analysis showed that all three regions were characterized by ductile dimples. The source and radiation regions were mainly intergranular fractures characterized by tearing. The ductile dimples in the radiation region were smaller and shallower, as shown in Figure 15c. There were clear serpentine slip patterns in the dimples of the shear lip region, as shown in Figure 15d.

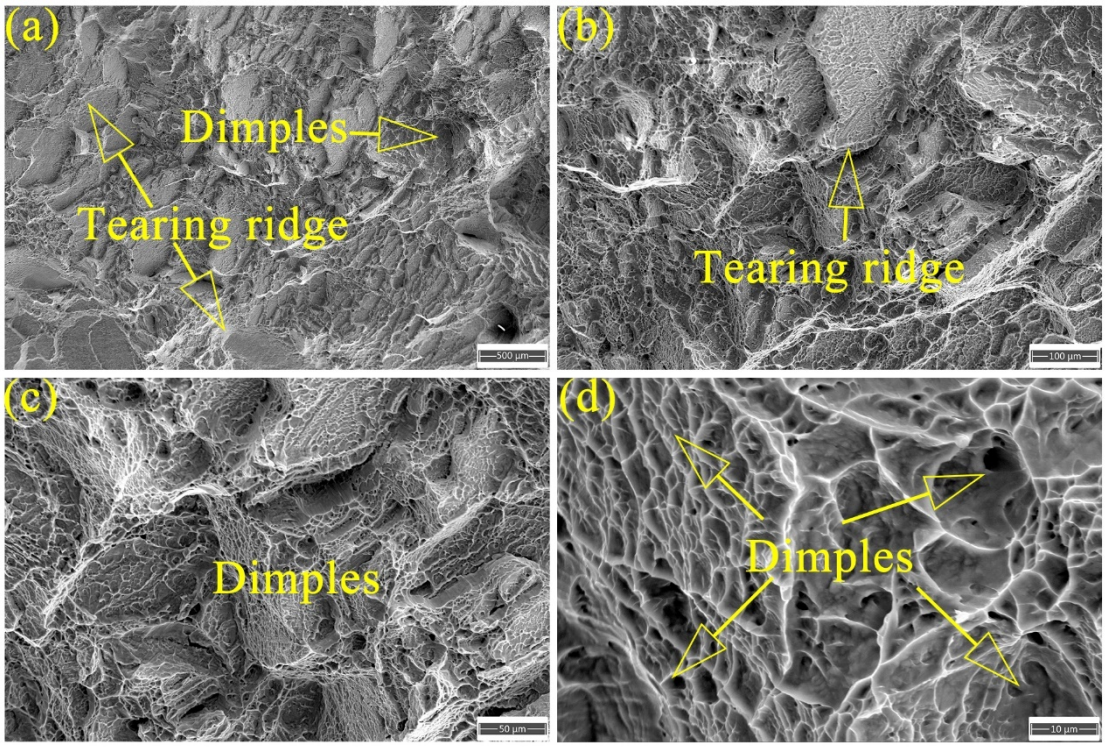

Figure 13. Morphologies of the tensile fracture surface. (**a**) typical ductile fracture characteristics; (**b**) tearing ridges characteristics; (**c**) typical dimples characteristics; (**d**) enlarged view of dimples characteristics. (Experimental parameters: P = 3.0 kW, v = 1.2 m/min, F = +20 mm).

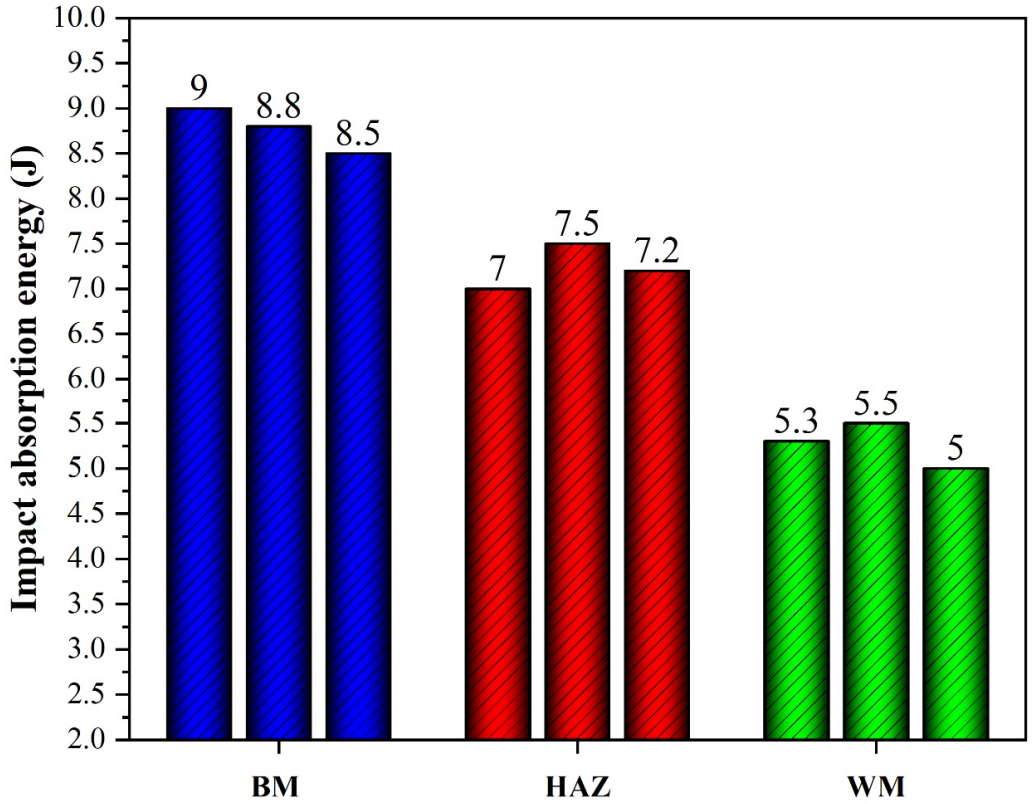

Figure 14. Impact properties of welded joints at different notch positions. (Experimental parameters: P = 3.0 kW, v = 1.2 m/min, F = +20 mm).

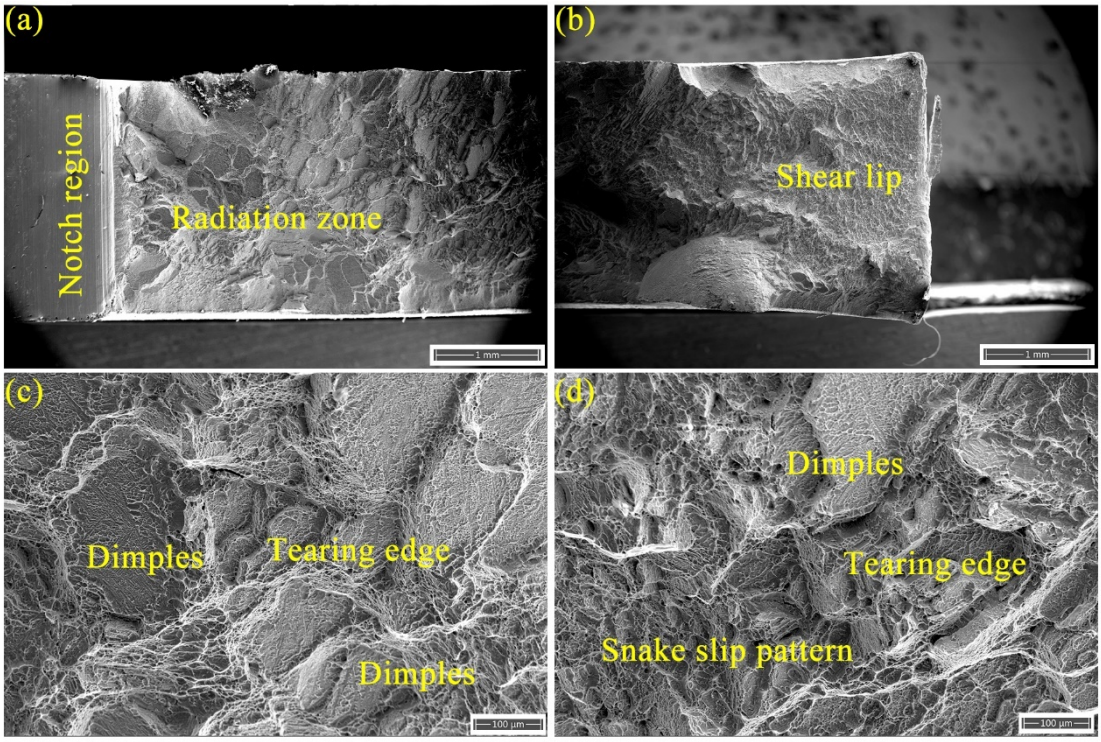

Figure 15. Impact fracture morphology of the weld metal. (**a**) notch region and radiation zone of the macroscopic fracture surface; (**b**) shear lip region of the macroscopic fracture surface; (**c**) enlarged view of the radiation region; (**d**) enlarged view of the shear lip region (Experimental parameters: P = 3.0 kW, v = 1.2 m/min, F = +20 mm).

4. Conclusions

(1) The laser welding of TA15 titanium alloy achieved good weld formation, with successful and flat weld formation, and there were no internal pores, cracks, incomplete penetration, or other defects.

(2) The base material was a typical α + β bimodal structure, with the α phase accounting for approximately 14.7%. HAZ was composed of parallel layer α phases in the transformation where the β group dissolved, and the interior of the equiaxed α was transformed towards a short rod shape. WM presented a typical basket-weave microstructure consisting of a large number of α′ martensitic phases and a small number of high-temperature residual β phases. The internal α′ martensitic phase had a high aspect ratio, and the layer α phases were deformable bodies with different Bulger orientation relationships.

(3) The microhardness of the welded joint was distributed in a hump distribution, gradually increasing from BM to HAZ. The microhardness of the fusion line was the highest at 454 HV. The hardness of the welded metal zone fluctuated between 410 and 450 HV, which was higher than that in the base metal area. The microhardness value of BM was the lowest at about 340 HV because a large number of needle-like α′ martensites, with high dislocation density and twinning, were formed in the welded metal zone.

(4) The ultimate tensile strength of the welded joint was 1006 ± 8.5 MPa (yield strength 935 MPa, the elongation 13% ± 1.2%), and the tensile strength of BM was 994 MPa (yield strength 931 MPa, the elongation 14% ± 0.8%). The fracture location was located in the base metal area, and the fracture morphology showed equiaxed dimples of varying sizes in a ductile fracture mode. The impact absorption energy of BM was higher than that of HAZ and WM. The weld metal zone had the lowest impact performance (5.3 J) since the weld metal was mainly composed of a large number of α′ martensitic phases.

(5) This shows that laser welding TA15 titanium alloy can produce good weldability and mechanical properties in lightweight aerospace components. The fatigue and durability performance of laser-welded TA15 titanium alloy joints are the main aspects that should be focused on in future investigations.

Author Contributions: S.Z.: Conceptualization, Methodology, Writing—Original draft, Writing—Review and Editing, Data curation; B.C.: Methodology, Writing—Review and Editing, Supervision; Z.Z.: Investigation, Writing—Review and Editing; Y.L.: Conceptualization, Writing—Review and Editing, Data curation; L.C.: Writing—Review and Editing, Supervision. All authors have read and agreed to the published version of the manuscript.

Funding: This research received no funding.

Data Availability Statement: The original contributions presented in the study are included in the article; further inquiries can be directed to the corresponding author.

Conflicts of Interest: The authors declare that they have no known competing financial interests or personal relationships.

References

1. Banerjee, D.; Williams, J.C. Perspectives on Titanium Science and Technology. *Acta Mater.* **2013**, *61*, 844–879. [CrossRef]
2. Zhang, D.; Qiu, D.; Gibson, M.A.; Zheng, Y.; Fraser, H.L.; StJohn, D.H.; Easton, M.A. Additive manufacturing of ultrafine-grained high-strength titanium alloys. *Nature* **2019**, *576*, 91–95. [CrossRef] [PubMed]
3. Zhang, R.; Xu, K.; Sun, F.; Ma, Z.; Huang, L.; Bolzoni, L.; Geng, L.; Yang, F. Achieving highly variable mechanical behaviors in TiBw/TA15(Si) composite by microstructure manipulation. *Mater. Charact.* **2024**, *212*, 113978. [CrossRef]
4. Yao, W.; Li, X.; Wei, Q.; Fu, M.; Wang, B.; Pan, S. Oxidation behavior of TA15 titanium alloy at high-temperature and the effect on infrared emissivity. *J. Alloys Compd.* **2024**, *983*, 173707. [CrossRef]
5. Rizwan, M.; Lu, J.; Ullah, R.; Zhang, Y.; Zhang, Z. Microstructural and texture evolution investigation of laser melting deposited TA15 alloy at 500 °C using in-situ EBSD tensile test. *Mater. Sci. Eng. A* **2022**, *857*, 144062. [CrossRef]
6. Ji, R.; Zhu, K.; Zhang, H.; Luo, H.; Mao, J. Microstructure evolution, mechanical response and strengthening models for TA15 titanium alloy during thermal processes: A brief review. *J. Mater. Res. Technol.* **2024**, *28*, 1644–1656. [CrossRef]
7. Zhu, S.; Yang, H.; Guo, L.G.; Fan, X.G. Effect of cooling rate on microstructure evolution during α/β heat treatment of TA15 titanium alloy. *Mater. Charact.* **2012**, *70*, 101–110. [CrossRef]
8. Yu, J.; Cai, C.; Xie, J.; Chen, Z.; Chen, H. Keyhole stability, arc behavior, and molten pool flow in narrow-gap oscillating laser-arc hybrid welding of titanium alloy. *Int. J. Heat Mass Transf.* **2024**, *220*, 124922. [CrossRef]
9. Deng, A.; Chen, H.; Zhang, Y.; Meng, Y.; Liu, Y.; Zeng, Y.; Liu, H.; Zhang, Z.; Zhang, M. Enhanced strength and ductility of aluminum alloy laser welded joints through Ca micro-alloyed welding materials. *Mater. Sci. Eng. A* **2024**, *900*, 146482. [CrossRef]
10. Gao, F.; Cui, Y.; Lv, Y.; Yu, W.; Jiang, P. Microstructure and properties of Ti–6Al–4V alloy welded joint by keyhole gas tungsten arc welding. *Mater. Sci. Eng. A* **2021**, *827*, 142024. [CrossRef]
11. Acherjee, B. Hybrid laser arc welding: State-of-art review. *Opt. Laser Technol.* **2018**, *99*, 60–71. [CrossRef]
12. Xu, C.; Liu, H.Q.; Li, C.H.; Yang, H.J.; Shao, X.H.; Ma, X.L. Internal tensile properties of characteristic zones in the electron beam weldment of TC17 titanium alloy. *Mater. Sci. Eng. A* **2023**, *875*, 145087. [CrossRef]
13. Atabaki, M.M.; Yazdian, N.; Ma, J.; Kovacevic, R. High power laser welding of thick steel plates in a horizontal butt joint configuration. *Opt. Laser Technol.* **2016**, *83*, 1–12. [CrossRef]
14. Xu, C.; Shao, X.H.; Yang, H.J.; Lv, M.; Liu, H.Q.; Ma, X.L. Uncovering the hierarchical clusters in the heat-affected zone of an electron beam welded α/β titanium alloy joint. *J. Mater. Sci. Technol.* **2024**, *174*, 120–132. [CrossRef]
15. Li, G.; Wang, Y.; Liang, Y.; Gao, P.; Liu, X.; Xu, W.; Yang, D. Microstructure and mechanical properties of laser welded Ti-6Al-4V (TC4) titanium alloy joints. *Opt. Laser Technol.* **2024**, *170*, 110320. [CrossRef]
16. Li, F.S.; Wu, L.H.; Zhao, H.B.; Xue, P.; Ni, D.R.; Xiao, B.L.; Ma, Z.Y. Realizing deep penetration and superior mechanical properties in a titanium alloy thick plate joint via vacuum laser beam welding. *J. Mater. Res. Technol.* **2023**, *26*, 2254–2264. [CrossRef]
17. Lei, Z.; Cao, H.; Cui, X.; Ma, Y.; Li, L.; Zhang, Q. A novel high efficiency narrow-gap laser welding technology of 120 mm high-strength steel. *Opt. Lasers Eng.* **2024**, *178*, 108232. [CrossRef]
18. Zhang, J.X.; Xue, Y.; Gong, S.L. Residual welding stresses in laser beam and tungsten inert gas weldments of titanium alloy. *Sci. Technol. Weld. Join.* **2005**, *10*, 643–646. [CrossRef]
19. Xie, J. Plasma fluctuation and keyhole instability in laser welding. In Proceedings of the ICALEO® '99: Proceedings of the Laser Materials Processing Conference, San Diego, CA, USA, 15–18 November 1999.
20. Deng, C.Y.; Liu, C.; Gong, B.M.; Zhang, C.Z.; Chang, L.I.U.; Yong, L.I.U. Effect of microstructure inhomogeneity on mechanical properties of different zones in TA15 electron beam welded joints. *Trans. Nonferrous Met. Soc. China* **2020**, *30*, 678–687. [CrossRef]
21. Zhan, X.; Peng, Q.; Wei, Y.; Ou, W. Experimental and simulation study on the microstructure of TA15 titanium alloy laser beam welded joints. *Opt. Laser Technol.* **2017**, *94*, 279–289. [CrossRef]

22. Xu, W.; Lui, E.W.; Pateras, A.; Qian, M.; Brandt, M.J.A.M. In situ tailoring microstructure in additively manufactured Ti-6Al-4V for superior mechanical performance. *Acta Mater.* **2017**, *125*, 390–400. [CrossRef]
23. Qian, M. Additive manufacturing of strong and ductile Ti–6Al–4V by selective laser melting via in situ martensite decomposition. *Acta Mater.* **2015**, *85*, 74–84.
24. Ohnishi, T.; Kawahito, Y.; Mizutani, M.; Katayama, S. Butt welding of thick, high strength steel plate with a high power laser and hot wire to improve tolerance to gap variance and control weld metal oxygen content. *Sci. Technol. Weld. Join.* **2013**, *18*, 314–322. [CrossRef]
25. Chen, X.; Zhang, X.; Pang, S.; Hu, R.; Xiao, J. Vapor plume oscillation mechanisms in transient keyhole during tandem dual beam fiber laser welding. *Opt. Lasers Eng.* **2018**, *100*, 239–247. [CrossRef]
26. Zhang, S.W.; Sun, J.H.; Zhu, M.H.; Zhang, L.; Nie, P.L.; Li, Z.G. Fiber laser welding of HSLA steel by autogenous laser welding and autogenous laser welding with cold wire methods. *J. Mater. Process. Technol.* **2020**, *275*, 116353. [CrossRef]
27. Frostevarg, J. Factors affecting weld root morphology in laser keyhole welding. *Opt. Lasers Eng.* **2018**, *101*, 89–98. [CrossRef]
28. Fan, J.; Zhao, D.; Chen, Z.; Zhang, Z.; Wang, J.; Tang, B.; Chen, Z.; Wang, Q.; Kou, H.; Li, J. Tailoring texture in a near-α titanium alloy: Insights from strain paths and cooling rate influences. *J. Mater. Res. Technol.* **2024**, *30*, 1388–1402. [CrossRef]
29. Liu, Y.; Wang, J.; Yan, T.; Yin, X.; Zhan, X. Effect of synchronous gas cooling method on microstructure and mechanical properties of laser welded joint for Ti6Al4V titanium alloy. *Mater. Today Commun.* **2024**, *39*, 108779. [CrossRef]
30. Gey, N.; Humbert, M. Specific analysis of EBSD data to study the texture inheritance due to the β → α phase transformation. *J. Mater. Sci.* **2003**, *38*, 1289–1294. [CrossRef]
31. Chen, X.; Zhang, J.; Chen, X.; Cheng, X.; Huang, Z. Electron beam welding of laser additive manufacturing Ti–6.5Al–3.5Mo–1.5Zr–0.3Si titanium alloy thick plate. *Vacuum* **2018**, *151*, 116–121. [CrossRef]
32. An, F.; Liu, X.; Zhang, H.; Zhang, L.; Ning, J.; Na, S.J. Comparison of performance of laser powder bed fusion thin-walled TC11 alloy samples welded via laser welding and electron beam welding. *Opt. Laser Technol.* **2024**, *170*, 110256. [CrossRef]
33. Farabi, E.; Hodgson, P.D.; Rohrer, G.S.; Beladi, H. Five-parameter intervariant boundary characterization of martensite in commercially pure titanium. *Acta Mater.* **2018**, *154*, 147–160. [CrossRef]
34. Wang, K.; Liu, G.; Zhao, J.; Wang, J.; Yuan, S. Formability and microstructure evolution for hot gas forming of laser-welded TA15 titanium alloy tubes. *Mater. Des.* **2016**, *91*, 269–277. [CrossRef]
35. Wang, S.C.; Aindow, M.; Starink, M.J. Effect of self-accommodation on α/α boundary populations in pure titanium. *Acta Mater.* **2003**, *51*, 2485–2503. [CrossRef]
36. Zhang, J.; Guo, H.; Hu, M.; Xu, H.; Ju, H.; Xu, D.; Teng, C.; Yang, R. Effect of common alloying elements on α′ martensite start temperature in titanium alloys. *J. Mater. Res. Technol.* **2023**, *27*, 4562–4572. [CrossRef]
37. Neelakantan, S.; Rivera-Díaz-del-Castillo, P.E.J.; Zwaag, S.V.D. Prediction of the martensite start temperature for β titanium alloys as a function of composition. *Scr. Mater.* **2009**, *60*, 611–614. [CrossRef]
38. Wang, S.; Li, W.; Chen, C. Microstructure and mechanical properties in ultrasonic-magnetic field coaxial hybrid GTAW joints of Ti-6Al-4V. *J. Manuf. Process.* **2024**, *120*, 795–808. [CrossRef]
39. *GB/T 2650-2008/ISO 9016:2001*; Destructive Tests on Welds in Metallic materialsimpact Tests-Test Specimen Location, Notch Orientation and Examination. Standardization Administration of the Peolple's Republic of China: Beijing, China, 2008.
40. Zhan, X.; Yan, T.; Gao, Q.; Zhu, Z.; Bu, H.; Wang, Z. The porosity formation mechanism in the laser welded joint of TA15 titanium alloy. *Mater. Res. Express* **2019**, *6*, 076558. [CrossRef]
41. Abdel-Hady, M.; Hinoshita, K.; Morinaga, M. General approach to phase stability and elastic properties of β-type Ti-alloys using electronic parameters. *Scr. Mater.* **2006**, *55*, 477–480. [CrossRef]